

Real-time dual-wavelength digital holographic microscopy for extended measurement range with enhanced axial resolution

Jonas Kühn^a, Tristan Colomb^b, Christophe Pache^a, Florian Charrière^a, Frédéric Montfort^c,
Etienne Cuche^c, Yves Emery^c, Pierre Marquet^b and Christian Depeursinge^a

^aEcole polytechnique fédérale de Lausanne, Institute of imaging and applied optics, 1015
Lausanne, Switzerland;

^bCentre de Neurosciences Psychiatriques, Département de psychiatrie DP-CHUV, Site de Cery,
1008 Prilly-Lausanne, Switzerland;

^cLyncée Tec SA, PSE-A, 1015 Lausanne, Switzerland

ABSTRACT

We report on advanced dual-wavelength digital holographic microscopy (DHM) methods, enabling single-acquisition real-time micron-range measurements while maintaining single-wavelength interferometric resolution in the nanometer regime. In top of the unique real-time capability of our technique, it is shown that axial resolution can be further increased compared to single-wavelength operation thanks to the uncorrelated nature of both recorded wavefronts. It is experimentally demonstrated that DHM topographic investigation within 3 decades measurement range can be achieved with our arrangement, opening new applications possibilities for this interferometric technique.

Keywords: Digital holography, dual-wavelength, two-wavelengths, beat-wavelength, phase microscopy

1. INTRODUCTION

Digital Holographic Microscopy (DHM) is a new fast-developing microscopy technique enabling realtime complex 3D reconstruction of the wavefront diffracted by a sample, from a single hologram recorded with a digital camera [1–4]. This numerical reconstruction presents several advantages including particularly the capability to digitally propagate the wavefront (numerical focus) and to numerically compensate for all optical aberrations [5–7]. Moreover, due to the interferometric nature of DHM and the original numerical reconstruction procedure, the quantitative phase information permits to achieve nanometer-range axial sensitivity [8], while transverse resolution remains diffraction-limited by the numerical aperture of the microscope objective. Typical nowadays applications requesting nanometer topographic precision range from micro-lenses investigations [9], moving micro-electro-mechanical systems (MEMS) monitoring up to MHz-range frequencies [10,11] to complex micro-structures characterization [12].

However, despite all these advantages, the periodic nature of the phase information results in a so-called phase ambiguity when objects with optical path lengths (OPL) larger than the laser wavelength (400-700 nm for the visible range) are considered. For a vast majority of situations, so-called unwrapping algorithms can be used to retrieve the true topography, but they may fail for high aspect-ratio structures (e.g. a step) or high-roughness surfaces. In such cases, DHM applications range is limited to small OPL samples, about half the wavelength in topology. Recently, we proposed in Ref. 13 a novel technique to get rid of this limitation, combining the well-known sequential-acquisitions two-wavelengths approach in DHM [14–16] with an exclusive single-shot hologram recording procedure to conserve the real-time advantage of DHM. This approach, based on multiple-wavelengths spatial multiplexing of the hologram, enables video-rate dual-wavelength DHM imaging with an extended measurement range in the tens of micrometers. By preserving the real-time feature, the method of Ref. 13 is fully adapted to moving sample investigation, and still compatible with stroboscopic operations mode for accessing high frequencies movements.

Further author information: (Send correspondence to Jonas Kühn)
E-mail: jonas.kuehn@a3.epf.ch, Telephone: +41 21 693 51 34

In addition to this method, we present here an algorithm to preserve the single-wavelength nanometer-range axial precision, while working in two-wavelength mode, thus reaching more than 3 decades measurement range for DHM. Finally, we demonstrate that not only the single-wavelength resolution can be conserved while working in dual-wavelength mode, but that it can be furthermore enhanced by a 20 to 30 % factor thanks to the simultaneous recording of two uncorrelated wavefronts.

2. PRINCIPLE OF SINGLE-ACQUISITION DUAL-WAVELENGTH DHM

In order to achieve single-acquisition dual-wavelength DHM as in Ref. [13], the hologram is acquired by a digital camera with two collinear object beams \mathbf{O}_1 and \mathbf{O}_2 at two different wavelengths λ_1 and λ_2 interfering with their two reference beams counterparts \mathbf{R}_1 and \mathbf{R}_2 , emitted by the same pair of laser sources, in an orthogonal off-axis configuration (slight angle between objects and reference beams, the last ones laying in orthogonal planes), as illustrated in Fig.1(a).

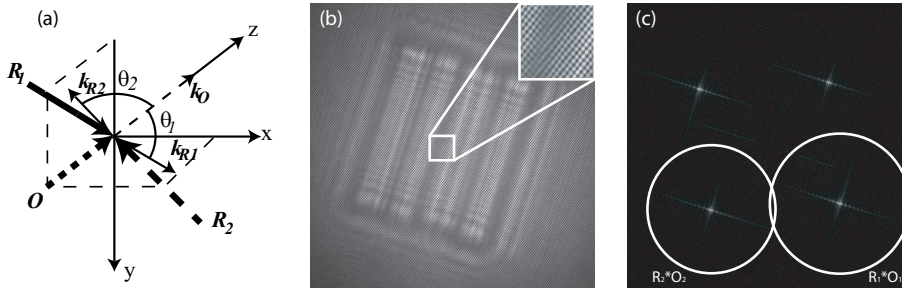


Figure 1. (a) 3D distribution of the incident waves propagation directions upon the CCD plane, k_{R1} and k_{R2} are the propagation direction vector of the reference waves \mathbf{R}_1 for wavelength λ_1 and \mathbf{R}_2 for λ_2 , and k_O is the one for the combined object waves; (b) Two-wavelengths spatially-multiplexed hologram with the inset representing a zoom on the central fringes, where the orthogonal spatial frequencies can be seen; (c) Fourier-spectrum of (b) (the zero order is filtered), where the virtual images for each wavelength can be separately spatial-filtered

The intensity of the recorded hologram of Fig.1(b), results from an incoherent addition of both interferograms at λ_1 and λ_2 that can be written as in Eq. 1.

$$I_H(x, y) = |\mathbf{R}_1|^2 + |\mathbf{O}_1|^2 + |\mathbf{R}_2|^2 + |\mathbf{O}_2|^2 + \mathbf{R}_1 \mathbf{O}_1^* + \mathbf{R}_1^* \mathbf{O}_1 + \mathbf{R}_2 \mathbf{O}_2^* + \mathbf{R}_2^* \mathbf{O}_2, \quad (1)$$

with I_H being the hologram intensity, x , y the coordinates in the camera plane and $*$ denoting the complex conjugate.

In Eq. 1 the first four intensity terms are the zero order, which can be automatically filtered in the Fourier domain [17], and the last four are the interference terms with the object wavefronts \mathbf{O}_i (the virtual images), or their conjugate \mathbf{O}_i^* (the real images), being modulated by the interference fringes spatial frequency (the carrier frequency) in the spatial frequency domain. With the object beams \mathbf{O}_i collinear on the optical axis, these carrier frequencies are dependent on the k-vectors of \mathbf{R}_1 and \mathbf{R}_2 . Now with the two references waves having orthogonal propagation directions as in Fig. 1(a), each interference term occupies different positions in the Fourier domain as illustrated in Fig. 1(c). In this configuration, it is possible to select each wavefront (usually the virtual images) by spatial filtering like in Fig. 1(c), and then to numerically propagate them in parallel. Writing the two associated filtered holograms as $I_{H,1}^F$ for $\mathbf{R}_1^* \mathbf{O}_1$ and $I_{H,2}^F$ for $\mathbf{R}_2^* \mathbf{O}_2$ and by using the convolution formulation, we have the expression of Eq. 2 for the propagation in the Fresnel approximation.

$$\Psi_{\text{CF},i}(m, n) = \Gamma_i^I(m, n) \cdot \frac{\exp(i2\pi d_i/\lambda_i)}{i\lambda_i d_i} \cdot \text{FFT}^{-1} \left\{ \text{FFT} [\Gamma_i^H(k, l) I_{H,i}^F(k, l)] \cdot \exp \left\{ -i\pi \lambda_i d_i \left[\left(\frac{k}{N\Delta x} \right)^2 + \left(\frac{l}{N\Delta y} \right)^2 \right] \right\} \right\}, \quad (2)$$

where $\Psi_{\text{CF},i}$ is the reconstructed wavefront for wavelength λ_i in the convolution formulation, Γ_i^I and Γ_i^H are digital phase masks (DPM) in the image plane and in the hologram plane respectively, used to compensate for aberrations (see Ref. [5] for details), d_i is the propagation distance for wavelength λ_i , FFT is the Fast Fourier Transform operator, (k, l) and (m, n) are the couple of integers so that $(-N/2 < k, l, m, n \leq N/2)$ representing coordinates in the hologram plane, respectively the reconstruction plane, $N \times N$ is the number of pixels of the CCD camera and Δx and Δy are the pixel sizes.

The formulation of Eq. 2 enables to propagate numerically each wavefront $\Psi_{\text{CF},i}$ in parallel and in an independent manner. Moreover, the DPMs can be adapted to compensate for each wavefront aberrations and the propagation distances d_i can be adjusted differently to compensate for slight chromatic aberrations or axial specimen displacement. In top of that, the DPMs could also serve as digital magnification lenses to match the image sizes in case of stronger chromatic aberrations [6]. The parallel propagations yield a reconstruction rate of about 7 frames per second with a standard dual-core PC at 2 GHz with 512x512 pixels holograms (roughly half the standard single-wavelength reconstruction rate). An a-posteriori hologram stack reconstruction can also be performed, and in this case is only limited by the acquisition rate of the CCD camera (here 25 frames per second).

After the digital wavefront propagation, $\mathbf{O}_1 \mathbf{O}_2^*$ can be computed in the reconstruction plane (focused image) in order to obtain the so-called synthetic beat-wavelength phase map, as expressed in Eq. 3:

$$\Phi = \arg(\mathbf{O}_1 \mathbf{O}_2^*) = \phi_1 - \phi_2 = 2\pi \frac{x}{\lambda_1} - 2\pi \frac{x}{\lambda_2} = 2\pi x \left(\frac{\lambda_2 - \lambda_1}{\lambda_1 \lambda_2} \right) = 2\pi \frac{x}{\Lambda}, \quad (3)$$

where x is the OPL (twice the topography in reflection, for an homogeneous sample in air), ϕ_i the reconstructed phase for the wavelength λ_i and Λ is the synthetic beat wavelength defined as:

$$\Lambda = \frac{\lambda_1 \lambda_2}{\|\lambda_2 - \lambda_1\|}. \quad (4)$$

Usually, the wavelength pair is chosen to render the beat-wavelength much larger than the original couple of wavelengths, as the smaller the difference $(\lambda_2 - \lambda_1)$, the larger the synthetic wavelength Λ , typically within the range of micrometers to millimeters. The corresponding synthetic phase obtained with Eq. 3 thus enables to resolve much higher structures by removing the phase ambiguity in the range of half the beat-wavelength Λ , thus greatly increasing the range for the phase measurement, while conserving the decisive single-acquisition feature.

However, though, in Eq. 3 the phase noise on ϕ_1 or ϕ_2 is roughly amplified by a factor Λ/λ_i when the synthetic phase Φ is converted in topography, typically 10-20 times higher. This drawback results in a loss of axial resolution when working with a dual-wavelength configuration, thus having to choose between high-resolution small-range single-wavelength DHM and low-resolution high-range dual-wavelength DHM. Nevertheless, it will be shown that, as long as the phase noise on ϕ_i lies within a reasonable range, it is possible to conserve - and even enhance - the interferometric resolution of single-wavelength DHM by using a simple algorithm.

3. MAINTAINING HIGH-RESOLUTION FOR DUAL-WAVELENGTH DHM

The goal here is to maintain the nanometer-scale resolution when working with the beat-wavelength generated by the two simultaneously-acquired wavefronts of wavelength λ_1 and λ_2 . This is usually achieved by using the beat-wavelength phase map Φ only to solve the phase ambiguity for one wavelength, then adding the correct integer multiple of 2π to the corresponding single-wavelength phase map ϕ_i , thus conserving the low-noise properties of it. This can be best described as a "dual-wavelength unwrapping" and such algorithms have already been used for sequential two-wavelengths DHM [4, 14, 15] for a while, and here we propose the floor-ceil implementation of Eq. 5 to retrieve the high-precision topographic map $z_i = OPL_i/2$ corresponding to wavelength λ_i .

$$\begin{aligned} z_{i,floor} &= \lfloor \frac{\Phi\Lambda}{2\pi\lambda_i} \rfloor \frac{\lambda_i}{2} + \frac{\phi_i}{4\pi} \lambda_i \\ z_{i,ceil} &= \lceil \frac{\Phi\Lambda}{2\pi\lambda_i} \rceil \frac{\lambda_i}{2} + \frac{\phi_i}{4\pi} \lambda_i \\ z_i &= \begin{cases} z_{i,floor} & \text{if } |\frac{\Phi\Lambda}{4\pi} - z_{i,floor}| < |\frac{\Phi\Lambda}{4\pi} - z_{i,ceil}| \\ z_{i,ceil} & \text{if } |\frac{\Phi\Lambda}{4\pi} - z_{i,floor}| > |\frac{\Phi\Lambda}{4\pi} - z_{i,ceil}| \end{cases} \end{aligned} \quad (5)$$

where $\lfloor \cdot \rfloor$ denotes the rounded value to the lower integer, $\lceil \cdot \rceil$ the one to the higher, and z are topographic values (half the OPL).

In Eq. 5, a comparison is done between the two possible results with both nearest integer multiples of the wavelength: this is done by checking which values is closest to the beat-wavelength topographic map. This algorithm enables to overcome the amplified phase error due to noise on ϕ_1 and ϕ_2 , as long as this amplified synthetic phase noise lays below the $\lambda_i/2$ threshold level. Let us express the condition for the synthetic phase noise Φ as in Eq. 6, with an amplified noise for the synthetic OPL_s map σ_{OPL_s} staying below $\lambda_i/2$ within a 99% probability, corresponding to 3σ for gaussian noise statistic.

$$3\sigma_{OPL_s} < \frac{\lambda_i}{2} \iff 3\sigma_{\Phi} \frac{\Lambda}{2\pi} < \frac{\lambda_i}{2} \quad (6)$$

Still assuming a gaussian noise distribution for both wavelength phase maps ϕ_1 and ϕ_2 , and making the hypothesis of similar noise levels ($\sigma_{\phi_1} = \sigma_{\phi_2} = \sigma_{\phi}$), the synthetic phase noise standard deviation obtained by subtracting ϕ_1 and ϕ_2 as in Eq. 3 should be amplified by a $\sqrt{2}$ factor:

$$\sigma_{\Phi} \approx \sqrt{2}\sigma_{\phi} \quad (7)$$

Inserting the expression of Eq. 7 in Eq. 6, we obtain the condition for phase noise ϕ_i to achieve dual-wavelength unwrapping as in Eq. 5 without introducing integer wavelength multiples errors:

$$\sigma_{\phi} < \frac{\pi}{3\sqrt{2}} \frac{\lambda_i}{\Lambda} \quad (8)$$

The condition of Eq. 8 enables to compute a high-precision phase map without phase ambiguity from the synthetic phase map Φ , with a 99% error-free rate under the hypothesis of similar amplitude uncorrelated gaussian noise for the single-wavelength phase maps ϕ_i . As can be expected, the higher the beat-wavelength Λ used, the smaller the phase noise should be to maintain nanometer-range precision. For examples, for a 680 nm range wavelength λ_i and a $\Lambda = 6.4 \mu\text{m}$ synthetic wavelength like in the configuration of Ref. 13, the condition of Eq. 8 is $\sigma_{\phi} < 4.5^\circ$. However if the synthetic wavelength is increased to about $\Lambda = 20 \mu\text{m}$, the phase noise condition restricts to $\sigma_{\phi} < 1.5^\circ$, which requests a very high setup quality.

At this point, assuming that the condition of Eq. 8 is fulfilled, the σ_{z_i} noise of topographic map obtained from Eq. 5 is of similar amplitude as the single wavelength noise $\lambda\sigma_{\phi_i}/4\pi$, usually in the 1-5 nm range depending on the sample and experimental conditions. However, it can be observed that two different topographic maps can

be simultaneously computed, z_1 with the unwrapping with λ_1 according to Eq. 5, and z_2 with λ_2 . Once again, by making the assumption of uncorrelated gaussian noise distribution of similar standard deviations σ_{zi} between the two wavefronts, it is possible to achieve a "spatial averaging" \bar{z} of both unwrapped topographic maps z_1 and z_2 with the following standard deviation property:

$$\sigma_{\bar{z}} \approx \frac{\sqrt{2}}{2} \sigma_{zi} \quad (9)$$

Thanks to the result of Eq. 9, it appears possible to gain an extra up to $\sqrt{2}/2$ factor for axial resolution over single-wavelength imaging in the same configuration, by computing the spatial average of the resulting dual-wavelength unwrapped topographic maps z_1 and z_2 . This can be seen as a way to "regain" the loss of resolution due to shot noise increase [18] for electron-well-limited configurations (most cases): indeed, here the photon number for each wavelength when acquiring simultaneously the pair of interferograms is reduced by a factor 2, compared to single-wavelength DHM, where the full CCD electron well capacity is exploited for a single interferogram recording. Consequently, the presented dual-wavelength configuration provides a very high measurement range, by combining the beat-wavelength information to discard phase ambiguity over several micrometers, and in addition the enhanced nanometer-range axial resolution as in Eq. 9, providing that the Eq. 8 condition is fulfilled.

4. RESULTS

To validate the technique, a purely-reflective object with abrupt steps of more than half a visible-range wavelength in height will be investigated. Such a specimen usually cannot be measured with monochromatic DHM because the phase ambiguity is nearly impossible to solve with the help of unwrapping algorithms, due to the step transitions compared to the lateral resolution. This sample is a micro-structured SiO₂ staircase on a Si wafer with a gold coating to ensure a perfect reflectivity. It consists in five steps with the following height values: 375, 525, 975, 1200, 1275 nm inducing up to 2.5 μm in term of OPL, which represents about four times a typical red-range wavelength and out of range of classical single-wavelength DHM. A schematic of this test-object and 3D experimentally reconstructed phase images, for simultaneously-acquired wavelengths $\lambda_1 = 680$ nm and $\lambda_2 = 760$ nm, of this sample from the hologram of Fig. 1(b) are presented in Fig. 2.

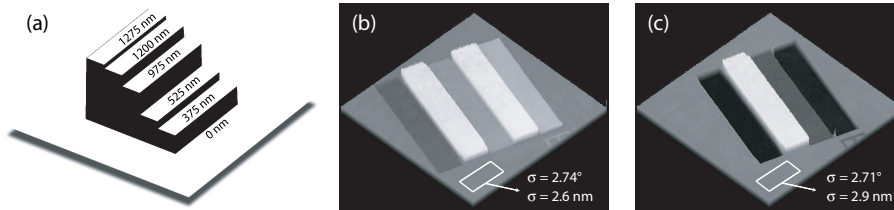


Figure 2. (a) Schematic of the staircase test-sample; (b,c) 3D representations of the reconstructed phase images ϕ_1 and ϕ_2 obtained with wavelengths $\lambda_1 = 680$ nm, respectively $\lambda_2 = 760$ nm, simultaneously acquired within the same hologram of Fig. 1(b). Standard deviations values are given on a flat sample area, both in nm and in $^\circ$.

The two 3D phase images of the staircase object in Fig. 2(b,c) illustrate well the phase ambiguity for single-wavelength imaging: the smallest step of 375 nm disappears in Fig. 2(c) because it corresponds to an OPL of 750 nm, which is nearly the value of $\lambda_2 = 760$ nm. This is a typical case where unwrapping algorithms are helpless. Hopefully, it is now possible to compute the beat-wavelength phase map according to Eq. 3 to remove the phase ambiguity, thus extending the measurement range to $\Lambda/2$. Figure 3 depicts the $\Lambda = 6.428$ μm synthetic wavelength topographic map obtained from the phase difference of Fig. 2(b,c), along with a transversal profile and the noise standard deviation value.

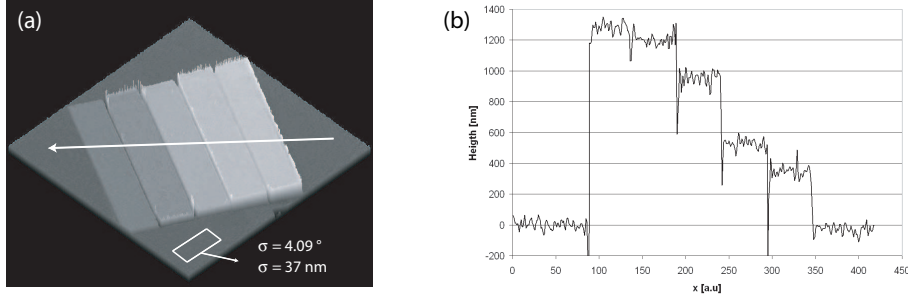


Figure 3. (a) Raw $\Lambda = 6.428 \mu\text{m}$ beat-wavelength topographic map z_s obtained from subtraction of the phase maps of Fig. 2(b,c), with the corresponding standard deviation values; (b) Profile line taken along the white line in (a), free of phase ambiguity

As can be observed in Fig. 3, the synthetic wavelength topographic map $z_s = \Phi\Lambda/4\pi$ is completely free of phase ambiguity for this up to $1.275 \mu\text{m}$ high sample, thus increasing the DHM measurement range as expected from this dual-wavelength configuration. However, the amplified noise phenomena is clearly illustrated with the standard deviation value being multiplied by about $\sqrt{2}$ regarding the phase (see Eq. 7) but especially when converted in topography it now corresponds to more than 35 nm due to the noise amplification! It results in a considerable drawback, as the measurement range gain comes along with nearly a factor 10 loss in axial resolution.

Anyway, as detailed in Eq. 5, the beat-wavelength OPL_s map corresponding to twice the topography z_s of Fig. 3(a) can thereafter be used only to unwrap one of the phase map ϕ_i , thus conserving the single-wavelength resolution. Indeed, as shown in Fig. 2(b,c), the phase noise in this experiment stands in the $2.5 - 3^\circ$ range which satisfy the Eq. 8 noise threshold condition. An example of such a dual-wavelength unwrapping is depicted in Fig. 4 with a $\lambda_1 = 680 \text{ nm}$ mapping.

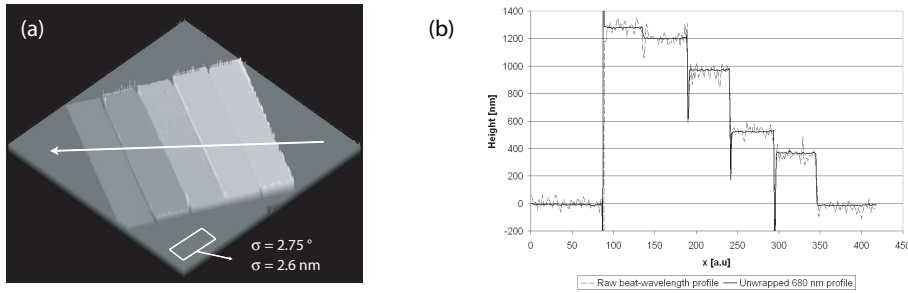


Figure 4. (a) High-resolution $\lambda_1 = 680 \text{ nm}$ topographic map z_1 obtained by dual-wavelength unwrapping of Fig. 2(b) with Fig. 3(a) according to Eq. 5, with the standard deviation values similar to single-wavelength imaging; (b) Profile line taken along the white line in (a), superposed with the raw beat-wavelength profile of Fig. 3(b), where the noise reduction can be clearly observed

Obviously, as demonstrated by the profile comparison in Fig. 4(b), the dual-wavelength unwrapping achieves at the same time micrometer range measurements and interferometric accuracy along the optical axis. As the noise condition of Eq. 8 is fulfilled, the standard deviation value σ_{z_1} of the unwrapped topographic map z_1 in Fig. 4(b) is quite exactly the same as with single-wavelength imaging in Fig. 2(b).

In addition to this, as demonstrated previously in Eq. 9, it is interesting to compute the average topographic map \bar{z} from the two unwrapped maps z_1 and z_2 , like z_1 in Fig. 4(a), because the gaussian noise property should induce a noise reduction due to the non-correlation between both wavelengths wavefronts. The resulting high-resolution topographic map \bar{z} is presented thereafter in Fig. 5.

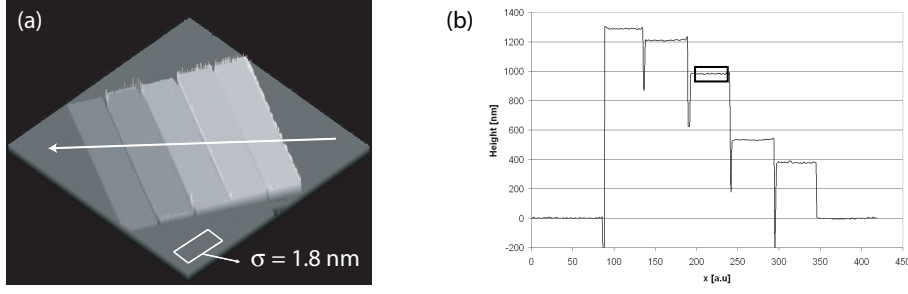


Figure 5. (a) Nanometer-resolution 3D topographic map \bar{z} obtained by spatial averaging of z_1 and z_2 , with the standard deviation value reduced by about 30 %; (b) Profile line taken along the white line in (a)

The obtained topographic standard deviation for $\sigma_{\bar{z}}$ on flat area of Fig. 5(a) is 1.8 nm, compared to 2.6 nm for σ_{z_1} in Fig. 4(a), corresponding to a noise reduction ratio of 0.69. This value is nearly $\sqrt{2}/2 = 0.71$ given in Eq. 9, expected for gaussian noise distributions averaging. It has been therefore possible to gain about 30% in axial reduction by using this novel approach. The enhanced image quality with \bar{z} can be best appreciated in Fig. 6, which is a zoomed profile on the 975 nm staircase corresponding to the black rectangle in Fig. 5(b) compared with the z_1 profile of Fig. 4(b).

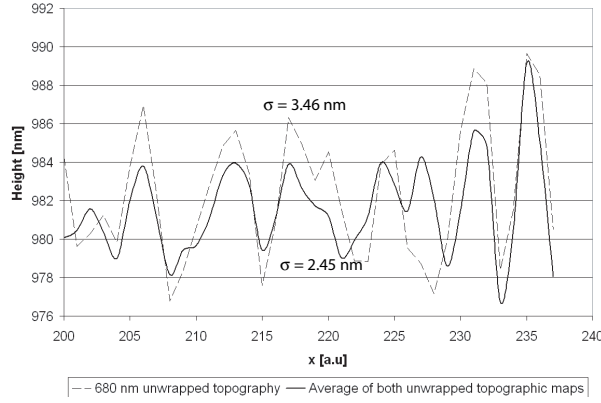


Figure 6. Comparison of zoomed portions of the profile line of Fig. 4(b) and Fig. 5(b) on the 975 nm step of the staircase sample corresponding to the black rectangle in Fig. 5(b), where the noise reduction can be best observable. The two profiles standard deviations in nm are also given.

5. CONCLUSION

We proposed a dual-wavelength digital holographic microscopy (DHM) technique achieving at the same time real-time monitoring (single camera acquisition), several micrometers measurement range without phase ambiguity, and interferometric axial resolution in the nanometer regime. The noise condition permitting this performance was studied, and experimental results on a test target validated the method. Furthermore, we presented a novel approach enabling to enhance even more the axial resolution by nearly 30%, by computing a spatial average between both simultaneously available uncorrelated wavefronts following a Gaussian noise distribution. Experimental validation of this method provided standard deviation value of less than 1.8 nm while working with a beat-wavelength measurement range of more than $3 \mu\text{m}$. Consequently, nanometer-precision DHM topographic investigation over more than 3 decades measurement range was demonstrated, thus opening a whole new range of applications possibilities for the technique.

The development of the technology has been supported by Swiss government through CTI grants TopNano 21 #6101.3 and NanoMicro #6606.2 and #7152.1. The author would also like to thank all the staff of Lyncee Tec SA (www.lynceetec.com) for their collaboration and the fruitful contributions.

REFERENCES

1. J. W. Goodman and R. W. Lawrence, "Digital image formation from electronically detected holograms," *Applied Physics Letters* **11**(3), pp. 77–79, 1967.
2. U. Schnars and W. Jüptner, "Direct recording of holograms by a ccd target and numerical reconstruction," *Applied Optics* **33**(2), pp. 179–181, 1994.
3. E. CuChe, F. Bevilacqua, and C. Depeursinge, "Digital holography for quantitative phase-contrast imaging," *Optics Letters* **24**(5), pp. 291–293, 1999.
4. U. Schnars and W. P. O. Juptner, "Digital recording and numerical reconstruction of holograms," *Measurement Science and Technology* **13**(9), pp. R85–R101, 2002.
5. T. Colomb, E. CuChe, F. Charrière, J. Kühn, N. Aspert, F. Montfort, P. Marquet, and C. Depeursinge, "Automatic procedure for aberration compensation in digital holographic microscopy and applications to specimen shape compensation," *Applied Optics* **45**(5), pp. 851–863, 2006.
6. T. Colomb, F. Montfort, J. Kühn, N. Aspert, E. CuChe, A. Marian, F. Charrière, S. Bourquin, P. Marquet, and C. Depeursinge, "Numerical parametric lens for shifting, magnification and complete aberration compensation in digital holographic microscopy," *Journal of the Optical Society of America a-Optics Image Science and Vision* **23**(12), pp. 3177–3190, 2006.
7. F. Montfort, F. Charrière, T. Colomb, E. CuChe, P. Marquet, and C. Depeursinge, "Purely numerical compensation for microscope objective phase curvature in digital holographic microscopy: influence of digital phase mask position," *Journal of the Optical Society of America a-Optics Image Science and Vision* **23**(11), pp. 2944–2953, 2006.
8. E. CuChe, P. Marquet, and C. Depeursinge, "Simultaneous amplitude-contrast and quantitative phase-contrast microscopy by numerical reconstruction of fresnel off-axis holograms," *Applied Optics* **38**(34), pp. 6994–7001, 1999.
9. F. Charrière, J. Kühn, T. Colomb, F. Montfort, E. CuChe, Y. Emery, K. Weible, P. Marquet, and C. Depeursinge, "Characterization of microlenses by digital holographic microscopy," *Applied Optics* **45**(5), pp. 829–835, 2006.
10. G. Coppola, P. Ferraro, M. Iodice, S. De Nicola, A. Finizio, and S. Grilli, "A digital holographic microscope for complete characterization of microelectromechanical systems," *Measurement Science and Technology* **15**(3), pp. 529–539, 2004.
11. F. Montfort, Y. Emery, F. Marquet, E. CuChe, N. Aspert, E. Solanas, A. Mehdaoui, A. Ionescu, and C. Depeursinge, "Process engineering and failure analysis of mems and moems by digital holography microscopy (dhm)," in *Proceedings of SPIE - The International Society for Optical Engineering, Reliability, Packaging, Testing, and Characterization of MEMS/MOEMS VI* **6463**, (San Jose, CA), 2007.
12. J. Kühn, E. CuChe, Y. Emery, T. Colomb, F. Charrière, F. Montfort, M. Botkine, N. Aspert, and C. Depeursinge, "Measurements of corner cubes microstructures by high-magnification digital holographic microscopy - art. no. 618804," in *Optical Micro- and Nanometrology in Microsystems Technology*, C. Gorecki, A. K. Asundi, and W. Osten, eds., *Proceedings of the Society of Photo-Optical Instrumentation Engineers (Spie)* **6188**, pp. 18804–18804, Spie-Int Society Optical Engineering, (Bellingham), 2006.
13. J. Kühn, T. Colomb, F. Montfort, F. Charrière, Y. Emery, E. CuChe, P. Marquet, and C. Depeursinge, "Real-time dual-wavelength digital holographic microscopy with a single hologram acquisition," *Optics Express* **15**(12), pp. 7231–7242, 2007.
14. J. Gass, A. Dakoff, and M. K. Kim, "Phase imaging without 2 pi ambiguity by multiwavelength digital holography," *Optics Letters* **28**(13), pp. 1141–1143, 2003.
15. D. Parshall and M. Kim, "Digital holographic microscopy with dual wavelength phase unwrapping," *Applied Optics* **45**(3), pp. 451–459, 2006.
16. I. Yamaguchi, T. Ida, M. Yokota, and K. Yamashita, "Surface shape measurement by phase-shifting digital holography with wavelength shift," *Applied Optics* **45**(29), pp. 7610–7616, 2006.
17. E. CuChe, P. Marquet, and C. Depeursinge, "Spatial filtering for zero-order and twin-image elimination in digital off-axis holography," *Applied Optics* **39**(23), pp. 4070–4075, 2000.
18. F. Charrière, B. Rappaz, J. Kühn, T. Colomb, P. Marquet, and C. Depeursinge, "Influence of shot noise on phase measurement accuracy in digital holographic microscopy," *Optics Express* **15**(14), pp. 8818–8831, 2007.